

(2021), 0, 0, pp. 1–29
doi:10.1093//Gao_etal2021

A Phylogenetic Approach to Inferring the Order in Which Mutations Arise during Cancer Progression

YUAN GAO*

Division of Biostatistics, The Ohio State University, 1958 Neil Ave, Columbus, OH 43210, US

gao.957@osu.edu

JEFF GAITHER

Institute for Genomic Medicine, Nationwide Children's Hospital, 700 Childrens Dr., Columbus, OH 43205,

US

JULIA CHIFMAN

Dept of Mathematics and Statistics, American University, 3501 Nebraska Ave NW, Washington 20016, US

LAURA KUBATKO

Mathematical Biosciences Institute, The Ohio State University, 1735 Neil Ave, Columbus, OH 43210, US

Depts of Statistics and Evolution, Ecology, and Organismal Biology, The Ohio State University, 1958 Neil Ave, Columbus, OH 43210, US

1 SUMMARY

2 Although the role of evolutionary process in cancer progression is widely accepted, increasing attention
3 is being given to the evolutionary mechanisms that can lead to differences in clinical outcome. Recent
4 studies suggest that the temporal order in which somatic mutations accumulate during cancer progression is
5 important. Single-cell sequencing provides a unique opportunity to examine the mutation order during cancer
6 progression. However, the errors associated with single-cell sequencing complicate this task. We propose a
7 new method for inferring the order in which somatic mutations arise within a tumor using noisy single-cell
8 sequencing data that incorporates the errors that arise from the data collection process. Using simulation, we

*To whom correspondence should be addressed.

9 show that our method outperforms existing methods for identifying mutation order in most cases, especially
10 when the number of cells is large. Our method also provides a means to quantify the uncertainty in the
11 inferred mutation order along a fixed phylogeny. We apply our method to empirical data from colorectal and
12 prostate cancer patients.

13 *Key words:* Bayesian inference; Cancer evolution; Error effects quantification; Mutation order; Single-cell sequencing.

14

1. INTRODUCTION

15 Cancer progression is a dynamic evolutionary process that occurs among the individual cells within each
16 patient's tumor. Cancer develops from a single cell in normal tissue whose genetic alterations endow a growth
17 advantage over the surrounding cells, allowing that cell to replicate and to expand, resulting in the formation
18 of a clonal population of identical cells. Cells within this clonal population may then undergo their own
19 somatic mutations, followed by replication and formation of subclones. During this complex process, many
20 competitive and genetically diverse subpopulations may be formed, resulting in intratumoral heterogeneity
21 (ITH) depicted in Fig. 1(a) (O'Sullivan *and others*, 2003; Ishwaran *and others*, 2009; Jamal-Hanjani *and*
22 *others*, 2017; Ascolani and Liò, 2019). Ortmann *and others* (2015) demonstrate that the type of malignancy
23 and the response to treatment of myeloproliferative neoplasm patients are affected by the order in which
24 somatic mutations arose within the patients' tumors. Though this study is specific to one type of cancer,
25 the timing and organization of somatic mutations are crucial to clinical outcomes for other cancers as well.
26 Determining the temporal order of mutations required for tumor progression is thus critical, especially in
27 the field of targeted therapy. However, this information cannot be observed directly, since genomic data are
28 most often collected at one snapshot in time. Consequently, use of computational methods that infer the
29 order of mutations from DNA sequence data is the approach of choice.

30 Most studies on cancer phylogenetics utilize bulk high-throughput sequencing data, but signals from
31 bulk sequencing only reflect the overall characteristics of a population of sequenced cells, rather than the
32 characteristics of individual cells. Variation in the mutational signatures among different cells in a tumor
33 is thus difficult to evaluate from bulk sequencing data. Single-cell sequencing (SCS) is promising because
34 it enables sequencing of individual cells, thus providing the highest possible resolution available on the
35 mutational history of cancer. However, the high error probabilities associated with SCS data complicate the

36 development of methods for inference of the mutational history. The whole-genome amplification (WGA)
37 process used to produce SCS data results in a variety of errors, including allelic dropout (ADO) errors, false
38 positives (FPs), non-uniform coverage distribution, and low coverage regions. ADO contributes a considerable
39 number of false negatives (FNs) to point mutations (Navin, 2014).

40 Recently, several studies have proposed various mathematical methods to infer mutation order (Fig. 1(c)
41 - Fig. 1(e)) from data arising from single-cell somatic mutations. Of particular interest are the methods of
42 Jahn *and others* (2016) and Zafar *and others* (2017), called SCITE and SiFit, respectively. SiFit uses an
43 MCMC approach as a heuristic to find the maximum likelihood tree from imperfect SCS data. Based on the
44 inferred tumor phylogenetic tree, SiFit estimates the mutation order by estimating the most likely mutation
45 states of the tips and the internal nodes using a dynamic programming algorithm. Although both SCITE and
46 SiFit by default output only the order of the mutations, both can be used to account for uncertainty in the
47 inferred order. For example, because SCITE uses an MCMC algorithm for inference, the posterior probability
48 associated with various mutation orders can be obtained by examining the frequency with which these orders
49 are sampled by the MCMC algorithm. Similarly, the authors of SiFit recently developed a method called
50 SiCloneFit (Zafar *and others*, 2019) that utilizes MCMC to sample trees, and thus the algorithm from SiFit
51 for inferring mutation order on a fixed tree could be applied to a posterior sample of trees to measure the
52 uncertainty in the mutation order that results from uncertainty in the tumor phylogeny.

53 In this paper, we propose a novel method for inferring the order in which mutations arise within an
54 individual tumor given SCS data from the tumor at a single time point. Our approach utilizes models
55 for both the mutational process within the tumor and the errors that arise during SCS data collection in
56 a Bayesian framework, thus allowing us to quantify the uncertainty in the inferred mutation order along
57 a fixed tumor phylogeny. Our approach thus represents a conceptually distinct and practically important
58 extension of earlier methods.

59 2. METHODS

60 We assume that we are given a phylogenetic tree with branch lengths that displays the evolutionary rela-
61 tionships among a sample of J cells within a tumor. To infer the locations (branches) on which a set of
62 somatic mutations are acquired in the tree, we need to model the evolutionary process of the somatic mu-

63 tations and quantify the technical errors that arise from the SCS data collection process. We assume that
64 during the evolutionary process, somatic mutations evolve independently across sites, and each mutation
65 evolves independently on different branches. We also assume that each somatic mutation occurs once along
66 the phylogeny and that no back mutation occurs, so that all descendant cells linked by the mutation branch
67 will harbor the corresponding mutation. When quantifying the effect of errors, we assume that SCS technical
68 errors for mutations are independent of one another.

69 **2.1 Notation and terminology**

70 Consider somatic mutations of interest at I loci across the genome for a sample of J single cells. The J
71 single cells are sampled from different spatial locations (clones) within the tumor. The mutation data can
72 be either binary or ternary. For binary data, 0 denotes the absence of mutation and 1 means that mutation
73 is present, while for ternary data, 0, 1 and 2 represent the homozygous reference (normal), heterozygous
74 (mutation present) and homozygous non-reference (mutation present) genotypes, respectively.

75 The I somatic mutations evolve along the tumor evolutionary tree \mathcal{T} . Each tip in \mathcal{T} represents one single
76 cell C_j , where $j = 1, \dots, J$. Let $C = \{C_1, \dots, C_J\}$ be the set of the J single cells under comparison. $\mathcal{T} = (T, \mathbf{t})$
77 includes two parts: the tree topology T and a vector of branch lengths \mathbf{t} . The tree topology $T = (V, E)$ is
78 a connected graph without cycles and is composed of nodes and branches, where V is the set of nodes and
79 E is the set of branches. Trees are rooted, and the root r represents the common ancestor (a normal cell
80 without somatic mutations) for all the single cells under comparison. In the context of this paper, all the
81 definitions in the following sections will apply to rooted bifurcating trees. There are $2J - 2$ branches in a
82 rooted bifurcating tree with J tips, i.e., $E = \{e_1, e_2, \dots, e_{2J-2}\}$. Let v and w be two nodes in the node set V
83 that are connected by the branch x in the branch set E (i.e., $x = \{v, w\}$: v is the immediate ancestor node of
84 w , and x connects v and w). Then the set $U^x(w)$, which includes the node w and all nodes descended from
85 w in \mathcal{T} , is called the *clade induced by w* . The branch x connects the ancestor node v and the clade induced
86 by w , and we define branch x as the *ancestor branch of clade $U^x(w)$* . $E^x(w)$ is a subset of E that includes
87 branches connecting nodes in $U^x(w)$, and $C^x(w)$ are the tips in $U^x(w)$.

88 Let G_{ij} denote the true genotype for the i^{th} genomic site of cell C_j . The i^{th} genomic site will then have
89 a vector $\mathbf{G}_i \in \{0, 1\}^J$ (for binary data) or $\{0, 1, 2\}^J$ (for ternary data) representing its true genotype for

90 all the J cells represented by the tips in the tree, where $i = 1, \dots, I$. Let S_{ij} denote the observed data for
 91 the i^{th} genomic site of cell C_j . Due to the technical errors associated with SCS data, the observed data
 92 S_{ij} does not always equal the true genotype G_{ij} . For both binary and ternary data, the observed state S_{ij}
 93 might be flipped with respect to the true genotype G_{ij} due to FP or FN. Missing states (“-”) or low-quality
 94 states (“?”) may be present for some genomic sites as well. Fig. 2 shows an example of true and observed
 95 binary genotype data for the mutations in Fig. 1. In Fig. 2, the observed state is highlighted in red if it is
 96 not consistent with the true genotype. The red numbers are those mutations with flipped observed mutation
 97 states relative to the true mutation states. The red dash (“-”) indicates a missing value and the red question
 98 mark (“?”) represents a low-quality value.

99 Mathematically, we represent the observed mutation states of the J single cells at I different genomic
 100 sites by an $I \times J$ mutation matrix \mathbf{S} for convenience,

$$\mathbf{S} = \begin{pmatrix} \mathbf{S}_1 \\ \mathbf{S}_2 \\ \vdots \\ \mathbf{S}_I \end{pmatrix} = \begin{pmatrix} S_{11} & \dots & S_{1J} \\ S_{21} & \dots & S_{2J} \\ \vdots & \ddots & \vdots \\ S_{I1} & \dots & S_{IJ} \end{pmatrix}. \quad (2.1)$$

101 Each entry (i, j) denotes the state observed for mutation i in cell C_j , so \mathbf{S}_i gives the observed data for genomic
 102 site i as a vector with J values corresponding to the J single cells. Column j represents the mutations of
 103 interest for cell C_j . In \mathcal{T} , let \mathcal{B} be the vector of locations (branches) on which the I mutations occur, i.e.,
 104 $\mathcal{B} = \{B_1, \dots, B_I\}$, where B_i is the branch on which mutation i is acquired. Note that B_i takes values in
 105 $\{e_1, e_2, \dots, e_{2J-2}\}$.

106 2.2 Somatic mutation process

107 To model the somatic mutation process, we consider continuous-time Markov processes, which we specify by
 108 assigning a rate to each possible transition between states. We consider point mutations. Once a mutation i
 109 is acquired on a branch $x \in E$, all the branches in the set $E^x(w)$ will harbor mutation i but those branches
 110 in the set $E \setminus (x \cup E^x(w))$ will not carry this mutation.

111 2.2.1 **Binary genotype data** For binary genotype data, the mutation process can be modeled by the
 112 2×2 transition rate matrix

$$\mathcal{Q}_\lambda = \begin{matrix} & 0 & 1 \\ \begin{matrix} 0 \\ 1 \end{matrix} & \begin{pmatrix} -\lambda & \lambda \\ 0 & 0 \end{pmatrix} \end{matrix}, \quad (2.2)$$

113 where λ denotes the instantaneous transition rate per genomic site. The transition probability matrix $P(t)$
 114 along a branch of length t is then computed by matrix exponentiation of the product of \mathcal{Q}_λ and the branch
 115 length t , which gives

$$P(t) = \begin{matrix} & 0 & 1 \\ \begin{matrix} 0 \\ 1 \end{matrix} & \begin{pmatrix} P_{00}(t) & P_{01}(t) \\ P_{10}(t) & P_{11}(t) \end{pmatrix} \end{matrix} = \begin{matrix} & 0 & 1 \\ \begin{matrix} 0 \\ 1 \end{matrix} & \begin{pmatrix} \exp(-\lambda t) & 1 - \exp(-\lambda t) \\ 0 & 1 \end{pmatrix} \end{matrix}. \quad (2.3)$$

116 Note that $P_{01}(t)$ is the probability that mutation i is acquired along a branch of length t . Under this
 117 model and recalling that each mutation evolves independently along different branches in \mathcal{T} , the marginal
 118 probability that mutation i is acquired on branch $x \in E$, denoted by $P(B_i = x | \mathcal{T}, \mathcal{Q}_\lambda)$, is thus given by

$$P(B_i = x | \mathcal{T}, \mathcal{Q}_\lambda) = \frac{\left[\prod_{B \in [E \setminus (x \cup E^x(w))]} P_{00}(t_B) \right] P_{01}(t_x) \left[\prod_{B \in E^x(w)} P_{11}(t_B) \right]}{\sum_{z \in E} \left(\left[\prod_{B \in [E \setminus (z \cup E^z(h))]} P_{00}(t_B) \right] P_{01}(t_z) \left[\prod_{B \in E^z(h)} P_{11}(t_B) \right] \right)}, \quad (2.4)$$

119 where t_B is length of branch B . In the numerator, the first term is a product of probabilities over all branches
 120 without the mutation, the second term is the probability that the mutation is acquired on branch x , and the
 121 third term is a product of probabilities over all branches with the mutation, i.e., all branches in $E^x(w)$. The
 122 denominator is needed to create a valid probability distribution over all possible branches, and is obtained
 123 by summing the numerator over all valid branches $z \in E$. The $P(B_i = x | \mathcal{T}, \mathcal{Q}_\lambda)$ term is normalized by
 124 the denominator because we exclude two possibilities: a mutation is not acquired on any branch in \mathcal{T} , or a
 125 mutation is acquired more than once on different branches in \mathcal{T} .

126 As an example, Fig. 2 (c) depicts the observed and true binary genotype for mutation $i = 1$ shown in
 127 Fig. 2 (a)-(b). The set of branches is $E = \{e_1, \dots, e_8\}$ and the corresponding set of branch lengths would
 128 be $\mathbf{t} = \{t_1, \dots, t_8\}$. If mutation i is acquired on branch e_1 , the cell descending along branch e_8 will not
 129 carry the mutation, while those descending from the blue branches would carry this mutation. The marginal
 130 probability that mutation $i = 1$ is acquired on branch e_1 would be proportional to its numerator, i.e.,
 131 $P(B_1 = e_1 | \mathcal{T}, \mathcal{Q}_\lambda) \propto P_{00}(t_8)P_{01}(t_1)[P_{11}(t_2)P_{11}(t_3)P_{11}(t_4)P_{11}(t_5)P_{11}(t_6)P_{11}(t_7)]$.

132 2.2.2 **Ternary genotype data** The mutation model for ternary data is complex and includes three pos-
 133 sible ways that mutation i occurs on a branch x in \mathcal{T} :

134 1. The status of mutation i transitions from $0 \rightarrow 1$ on a branch x and there is no further mutation at this
 135 genomic site in \mathcal{T} .

136 2. The status of mutation i transitions directly from $0 \rightarrow 2$ on a branch x in \mathcal{T} .

137 3. The status of mutation i transitions from $0 \rightarrow 1$ on a branch x and then transitions from $1 \rightarrow 2$ on a
 138 branch $y \in E^x(w)$ in \mathcal{T} .

139 We let B_i be the location at which mutation i occurs, $B_i^{0 \rightarrow 1}$ would be the branch on which mutation status
 140 transitions from 0 to 1, $B_i^{0 \rightarrow 2}$ is the branch on which mutation status transitions from 0 to 2, and $B_i^{1 \rightarrow 2}$ is
 141 the branch on which mutation status transitions from 1 to 2. If the mutation i occurs on branch x , all cells
 142 in $C^x(w)$ will carry 1 or 2 mutations. In other words, $G_{ij} = 1$ or 2 for all $C_j \in C^x(w)$ and $G_{ij} = 0$ for all
 143 $C_j \in C \setminus C^x(w)$. We define the transition rate matrix \mathcal{Q}_λ as

$$\mathcal{Q}_\lambda = \begin{matrix} & \begin{matrix} 0 & 1 & 2 \end{matrix} \\ \begin{matrix} 0 \\ 1 \\ 2 \end{matrix} & \begin{pmatrix} -(\lambda_1 + \lambda_1 \lambda_2) & \lambda_1 & \lambda_1 \lambda_2 \\ 0 & -\lambda_2 & \lambda_2 \\ 0 & 0 & 0 \end{pmatrix} \end{matrix}, \quad (2.5)$$

144 where λ_1 and λ_2 denote the instantaneous transition rates per genomic site of the transitions $0 \rightarrow 1$ and
 145 $1 \rightarrow 2$, respectively. Studies have provided evidence that direct mutation of $0 \rightarrow 2$ at rate $\lambda_1 \lambda_2$ is possible
 146 in principle, although it is extremely rare (Iwasa *and others*, 2004). If λ_2 is 0 in Expression (2.5), the model
 147 will be reduced to the infinite sites diploid model. The transition probability matrix $P(t) = \exp(\mathcal{Q}_\lambda t)$ is then
 148 given by

$$P(t) = \begin{matrix} & \begin{matrix} 0 & 1 & 2 \end{matrix} \\ \begin{matrix} 0 \\ 1 \\ 2 \end{matrix} & \begin{pmatrix} \exp(-(\lambda_1 + \lambda_1 \lambda_2)t) & \frac{\lambda_1(\exp(-(\lambda_1 + \lambda_1 \lambda_2)t) - \exp(-\lambda_2 t))}{\lambda_2 - (\lambda_1 + \lambda_1 \lambda_2)} & \frac{(\lambda_1 \lambda_2 - \lambda_2) \exp(-(\lambda_1 + \lambda_1 \lambda_2)t) + \lambda_1 \exp(-\lambda_2 t)}{\lambda_2 - (\lambda_1 + \lambda_1 \lambda_2)} + 1 \\ 0 & \exp(-\lambda_2 t) & 1 - \exp(-\lambda_2 t) \\ 0 & 0 & 1 \end{pmatrix} \end{matrix}. \quad (2.6)$$

149 The marginal probability that mutation i occurs on branch $x \in E$ for the three possible conditions is thus
 150 given by

$$P(B_i^{0 \rightarrow 1} = x | \mathcal{T}, \mathcal{Q}_\lambda) = \frac{Q(B_i^{0 \rightarrow 1} = x)}{\sum_{z_1 \in E} [Q(B_i^{0 \rightarrow 1} = z_1) + Q(B_i^{0 \rightarrow 2} = z_1) + \sum_{z_2} Q(B_i^{0 \rightarrow 1} = z_1, B_i^{1 \rightarrow 2} = z_2)]}, \quad (2.7)$$

$$P(B_i^{0 \rightarrow 2} = x | \mathcal{T}, \mathcal{Q}_\lambda) = \frac{Q(B_i^{0 \rightarrow 2} = x)}{\sum_{z_1 \in E} [Q(B_i^{0 \rightarrow 1} = z_1) + Q(B_i^{0 \rightarrow 2} = z_1) + \sum_{z_2} Q(B_i^{0 \rightarrow 1} = z_1, B_i^{1 \rightarrow 2} = z_2)]}, \quad (2.8)$$

$$P(B_i^{0 \rightarrow 1} = x, B_i^{1 \rightarrow 2} = y | \mathcal{T}, \mathcal{Q}_\lambda) = \frac{Q(B_i^{0 \rightarrow 1} = x, B_i^{1 \rightarrow 2} = y)}{\sum_{z_1 \in E} [Q(B_i^{0 \rightarrow 1} = z_1) + Q(B_i^{0 \rightarrow 2} = z_2) + \sum_{z_2} Q(B_i^{0 \rightarrow 1} = z_1, B_i^{1 \rightarrow 2} = z_2)]}, \quad (2.9)$$

151 where

$$Q(B_i^{0 \rightarrow 1} = x) = \left[\prod_{B \in [E \setminus (x \cup E^x(w))]} P_{00}(t_B) \right] P_{01}(t_x) \left[\prod_{B \in E^x(w)} P_{11}(t_B) \right], \quad (2.10)$$

152

$$Q(B_i^{0 \rightarrow 2} = x) = \left[\prod_{B \in [E \setminus (x \cup E^x(w))]} P_{00}(t_B) \right] P_{02}(t_x) \left[\prod_{B \in E^x(w)} P_{22}(t_B) \right], \quad (2.11)$$

153

$$Q(B_i^{0 \rightarrow 1} = x, B_i^{1 \rightarrow 2} = y) = \left[\prod_{B \in [E \setminus (x \cup E^x(w))]} P_{00}(t_B) \right] P_{01}(t_x) \left[\prod_{B \in [E^x(w) \setminus (y \cup E^y(b))]} P_{11}(t_B) \right] P_{12}(t_y) \left[\prod_{B \in E^y(b)} P_{22}(t_B) \right]. \quad (2.12)$$

154 We normalize the marginal probabilities to exclude scenarios in which mutations are acquired more than

155 once or in which mutations are not acquired in \mathcal{T} . As an example, Fig. S1 in the Supplementary Material

156 depicts the same mutation as in Fig. 2, but considers ternary data, leading to the following:

157 1. The marginal probability that mutation i transitions from $0 \rightarrow 1$ on branch e_1 is $P(B_i^{0 \rightarrow 1} = e_1 | \mathcal{T}, \mathcal{Q}_\lambda) \propto$

158 $P_{00}(t_8)P_{01}(t_1)[P_{11}(t_2)P_{11}(t_3)P_{11}(t_4)P_{11}(t_5)P_{11}(t_6)P_{11}(t_7)].$

159 2. The marginal probability that mutation i transitions from $0 \rightarrow 2$ on branch e_1 is $P(B_i^{0 \rightarrow 2} = e_1 | \mathcal{T}, \mathcal{Q}_\lambda) \propto$

160 $P_{00}(t_8)P_{02}(t_1)[P_{22}(t_2)P_{22}(t_3)P_{22}(t_4)P_{22}(t_5)P_{22}(t_6)P_{22}(t_7)].$

161 3. The marginal probability that mutation i transitions from $0 \rightarrow 1$ on e_1 , and from $1 \rightarrow 2$ on e_3 is

162 $P(B_i^{0 \rightarrow 1} = e_1, B_i^{1 \rightarrow 2} = e_3 | \mathcal{T}, \mathcal{Q}_\lambda) \propto P_{00}(t_8)P_{01}(t_1)P_{11}(t_2)P_{12}(t_3)P_{22}(t_4)P_{22}(t_5)P_{22}(t_6)P_{22}(t_7).$

163 The probability $P(B_i^{0 \rightarrow 1} = e_1, B_i^{1 \rightarrow 2} = e_3 | \mathcal{T}, \mathcal{Q}_\lambda)$ is the marginal probability that two mutations at the
 164 same site along the genome occur on two branches e_1 and e_3 , respectively. After the first mutation occurs
 165 on branch e_1 , the second mutation can occur on any branch except e_1 and e_8 .

166

2.3 Quantification of SCS errors

167 To account for FPs and FNs in the observed SCS data, our method applies the error model for binary and
 168 ternary data from Kim and Simon (2014), Jahn *and others* (2016), and Zafar *and others* (2017). Let α_{ij} be
 169 the probability of a false positive error and β_{ij} be the probability of a false negative error for genomic site i
 170 of cell C_j .

171 For binary data, if the true genotype is 0, we may observe a 1, which is a false positive error. If the
 172 true genotype is 1, we may observe a 0, which is a false negative error. The conditional probabilities of the
 173 observed data given the true genotype at genomic site i of cell C_j are

$$\mathbf{N}^{ij} = \begin{matrix} & S_{ij} = 0 & S_{ij} = 1 \\ \begin{matrix} G_{ij} = 0 \\ G_{ij} = 1 \end{matrix} & \begin{pmatrix} 1 - \alpha_{ij} & \alpha_{ij} \\ \beta_{ij} & 1 - \beta_{ij} \end{pmatrix} \end{matrix}, \quad (2.13)$$

174 where $\mathbf{N}_{01}^{ij} = P(S_{ij} = 1 | G_{ij} = 0) = \alpha_{ij}$, and other entries are defined similarly. Under the assumption that
 175 sequencing errors are independent, if mutation i is acquired on branch x , we can precisely quantify the effect
 176 of SCS technical errors for mutation i as

$$P(\mathbf{S}_i | B_i = x, \mathcal{T}, \mathbf{N}^i) = \prod_{j=1}^J P(S_{ij} | G_{ij}), \quad (2.14)$$

177 where $\mathbf{N}^i = \{\mathbf{N}^{i1}, \dots, \mathbf{N}^{iJ}\}$. Using the example in Fig. 2, the error probability of the observed genotype condi-
 178 tioning on the mutation $i = 1$ occurring on branch e_1 would be $P(\mathbf{S}_1 | B_1 = e_1, \mathcal{T}, \mathbf{N}^1) = \mathbf{N}_{11}^{11} \mathbf{N}_{10}^{12} \mathbf{N}_{11}^{13} \mathbf{N}_{10}^{14} \mathbf{N}_{00}^{15}$,
 179 where $\mathbf{N}^1 = \{\mathbf{N}^{11}, \dots, \mathbf{N}^{15}\}$ for this binary data example.

180 For ternary data, the conditional probabilities of the observed data given the true genotype are given by

$$\mathbf{N}^{ij} = \begin{matrix} & S_{ij} = 0 & S_{ij} = 1 & S_{ij} = 2 \\ \begin{matrix} G_{ij} = 0 \\ G_{ij} = 1 \\ G_{ij} = 2 \end{matrix} & \begin{pmatrix} 1 - \alpha_{ij} - \alpha_{ij}\beta_{ij}/2 & \alpha_{ij} & \alpha_{ij}\beta_{ij}/2 \\ \beta_{ij}/2 & 1 - \beta_{ij} & \beta_{ij}/2 \\ 0 & 0 & 1 \end{pmatrix} \end{matrix}, \quad (2.15)$$

181 where $\mathbf{N}_{01}^{ij} = P(S_{ij} = 1 | G_{ij} = 0) = \alpha_{ij}$, and the other entries are defined similarly. Under the same assump-

182 tions as for binary genotype data, we can precisely quantify the effect of SCS technical errors as in Equation
 183 (2.14) if mutation i is acquired on branch x . Using the example in Fig. S1 in the Supplementary Material,
 184 the error probabilities for the three possible ways that mutation $i = 1$ may arise on branch e_1 are

185 1. The error probability under the condition that the true mutation transitions from $0 \rightarrow 1$ on branch e_1
 186 is $P(\mathbf{S}_1|B_i^{0 \rightarrow 1} = e_1, \mathcal{T}, \mathbf{N}^1) = \mathbf{N}_{12}^{11} \mathbf{N}_{10}^{12} \mathbf{N}_{11}^{13} \mathbf{N}_{10}^{14} \mathbf{N}_{00}^{15}$.

187 2. The error probability under the condition that the true mutation transitions from $0 \rightarrow 2$ on branch e_1
 188 is $P(\mathbf{S}_1|B_i^{0 \rightarrow 2} = e_1, \mathcal{T}, \mathbf{N}^1) = \mathbf{N}_{22}^{11} \mathbf{N}_{20}^{12} \mathbf{N}_{21}^{13} \mathbf{N}_{20}^{14} \mathbf{N}_{00}^{15}$.

189 3. The error probability under the condition that the true mutation transitions from $0 \rightarrow 1$ on branch e_1 ,
 190 and transitions from $1 \rightarrow 2$ on branch e_3 is $P(\mathbf{S}_1|B_i^{0 \rightarrow 1} = e_1, B_i^{1 \rightarrow 2} = e_3, \mathcal{T}, \mathbf{N}^1) = \mathbf{N}_{12}^{11} \mathbf{N}_{20}^{12} \mathbf{N}_{21}^{13} \mathbf{N}_{20}^{14} \mathbf{N}_{00}^{15}$.

191 And $\mathbf{N}^1 = \{\mathbf{N}^{11}, \dots, \mathbf{N}^{15}\}$ for this ternary data example. The term $P(\mathbf{S}_1|B_i^{0 \rightarrow 1} = e_1, B_i^{1 \rightarrow 2} = e_3, \mathcal{T}, \mathbf{N}^1)$
 192 gives the error probability for the case in which the two mutations at the same genomic site occur on branches
 193 e_1 and e_3 .

194 2.4 *Missing and low-quality data*

195 In real data, missing and low-quality states are observed and must be taken into account. For each mutation
 196 i , we exclude cells with missing states, and a subtree \mathcal{T}_i from \mathcal{T} is extracted. The number of tips J_i in subtree
 197 \mathcal{T}_i is less than or equal to J . Let E_i be the set of branches in subtree \mathcal{T}_i . The probability that mutation
 198 i occurs on branch x is then given by $P(B_i = x|\mathcal{T}, \mathcal{Q}_\lambda) = P(B_i = x|\mathcal{T}_i, \mathcal{Q}_\lambda)$, where $P(B_i = x|\mathcal{T}_i, \mathcal{Q}_\lambda)$ is
 199 computed based on branches in the subtree \mathcal{T}_i , and $P(B_i = x|\mathcal{T}_i, \mathcal{Q}_\lambda)$ is 0 for those branches $x \in E \setminus E_i$. We
 200 quantify the effect of the SCS technical errors as

$$P(\mathbf{S}_i|B_i = x, \mathcal{T}, \mathbf{N}^i) = \prod_{j=1}^{J_i} \left(\sum_{S_{ijk}} w_{ijk} P(S_{ijk}|G_{ijk}) \right), \quad (2.16)$$

201 where w_{ijk} is the weight for each possible observed state at a mutation site. For a site with an observed
 202 state that is not missing or ambiguous, w_{ijk} is 1 for the observed state and 0 for all other states. For
 203 an ambiguous site, we can assign equal weight for each possible state, or we can assign weight based on
 204 sequencing information or other biological characteristics.

205 2.5 *Inferring the location of a mutation in \mathcal{T}*

206 Once the observed matrix $\mathbf{S} = [\mathbf{S}_1 \dots \mathbf{S}_I]^T$ of the I mutations has been collected, the next step is to infer the
 207 branch on which mutation i takes place, conditioning on \mathbf{S} . Given the observed data matrix \mathbf{S} , the tumor

208 phylogenetic tree \mathcal{T} , the error probability matrix $\mathbf{N} = \{\mathbf{N}^{ij} | 1 \leq i \leq I, 1 \leq j \leq J\}$, and the mutation process
 209 \mathcal{Q}_λ , we can assign a posterior probability distribution $P(B_i | \mathbf{S}, \mathcal{T}, \mathbf{N}, \mathcal{Q}_\lambda)$ to the location of mutation i using
 210 Bayes' theorem,

$$P(B_i = x | \mathbf{S}, \mathcal{T}, \mathbf{N}, \mathcal{Q}_\lambda) = \frac{P(\mathbf{S}_i | B_i = x, \mathcal{T}_i, \mathbf{N}^i) P(B_i = x | \mathcal{T}_i, \mathcal{Q}_\lambda)}{P(\mathbf{S}_i | \mathcal{T}_i, \mathbf{N}^i, \mathcal{Q}_\lambda)}. \quad (2.17)$$

211 For mutation i , $P(B_i = x | \mathbf{S}_i, \mathcal{T}_i, \mathbf{N}^i, \mathcal{Q}_\lambda)$ is computed for all x in set E_i . For example, there are 8 branches in
 212 the tree in Fig. 2, so the branch on which mutation $i = 1$ occurs, B_1 , can be any of the 8 branches. For the
 213 binary example, the posterior probability that mutation $i = 1$ occurs on e_1 is $P(B_1 = e_1 | \mathbf{S}_1, \mathcal{T}_1, \mathbf{N}^1, \mathcal{Q}_\lambda) \propto$
 214 $P_{00}(t_8) P_{01}(t_1) [P_{11}(t_2) P_{11}(t_3) P_{11}(t_4) P_{11}(t_5) P_{11}(t_6) P_{11}(t_7)] \cdot \mathbf{N}_{11}^{11} \mathbf{N}_{10}^{12} \mathbf{N}_{11}^{13} \mathbf{N}_{10}^{14} \mathbf{N}_{00}^{15}$. In this way, the posterior
 215 probability that the mutation occurs on each of the 8 branches can be computed, giving the probability
 216 distribution for the location of mutation $i = 1$, i.e. $P(B_1 = x | \mathbf{S}_1, \mathcal{T}_1, \mathbf{N}^1, \mathcal{Q}_\lambda)$ for $x \in \{e_1, \dots, e_8\}$.

217 To summarize this probability distribution, we construct a $(1 - \theta) \times 100\%$ credible set for the location of
 218 mutation i as follows. First, the branches are ranked by their posterior probabilities, and then branches are
 219 added to the credible set in the order of decreasing posterior probability until the sum of their probabilities
 220 reaches $(1 - \theta)$. The number of branches in the credible set is informative about the level of certainty
 221 associated with the inferred location for the mutation. To obtain a point estimate, we pick the branch that
 222 maximizes the posterior probability, i.e., the maximum a posteriori (MAP) estimate. The MAP estimator
 223 for the location of mutation i is given by

$$\hat{B}_{i_{MAP}} = \operatorname{argmax}_{B_i \in \{e_1, \dots, e_{2J-2}\}} P(B_i | \mathbf{S}_i, \mathcal{T}, \mathbf{N}^i, \mathcal{Q}_\lambda). \quad (2.18)$$

224 For the example in Fig. 2, the branch with the largest posterior probability is $\hat{B}_{1_{MAP}}$ for mutation $i = 1$.

225 2.6 Inferring the mutation order in \mathcal{T}

226 We now consider the joint posterior probability distribution of the locations for the I mutations in the sample
 227 of J single cells. Based on the assumption of independence among the I mutations being considered, the
 228 posterior distribution for \mathcal{B} is given by

$$P(\mathcal{B} | \mathbf{S}, \mathcal{T}, \mathbf{N}, \mathcal{Q}_\lambda) = \prod_{i=1}^I P(B_i | \mathbf{S}_i, \mathcal{T}, \mathbf{N}^i, \mathcal{Q}_\lambda), \quad (2.19)$$

229 where $\mathbf{N}^i = \{\mathbf{N}^{i1}, \dots, \mathbf{N}^{iJ}\}$. From this distribution, we can extract information on the ordering of mutations
 230 of interest. For example, if we are interested in the order of mutation $i = 1$ and mutation $i = 2$ in Fig. 2,

231 the joint posterior probability distribution that mutation $i = 1$ occurs on branch $x \in E$ and mutation $i = 2$
 232 occurs on branch $y \in E$ can be used to find the probability that mutation $i = 1$ occurs earlier in the tree than
 233 mutation $i = 2$. Note that $P^{B_1=x, B_2=y} = P(B_1 = x, B_2 = y | \mathbf{S}, \mathcal{T}, \mathbf{N}, \mathcal{Q}_\lambda) = P(B_1 = x | \mathbf{S}, \mathcal{T}, \mathbf{N}, \mathcal{Q}_\lambda) \cdot P(B_2 =$
 234 $y | \mathbf{S}, \mathcal{T}, \mathbf{N}, \mathcal{Q}_\lambda)$. This joint distribution can be represented in a matrix given by

$$\begin{matrix}
 & B_1 = e_1 & B_1 = e_2 & \dots & B_1 = e_8 \\
 \begin{matrix} B_2 = e_1 \\ B_2 = e_2 \\ \vdots \\ B_2 = e_8 \end{matrix} & \begin{pmatrix} P^{B_1=e_1, B_2=e_1} & P^{B_1=e_2, B_2=e_1} & \dots & P^{B_1=e_8, B_2=e_1} \\ P^{B_1=e_1, B_2=e_2} & P^{B_1=e_2, B_2=e_2} & \dots & P^{B_1=e_8, B_2=e_2} \\ \vdots & \vdots & \ddots & \vdots \\ P^{B_1=e_1, B_2=e_8} & P^{B_1=e_2, B_2=e_8} & \dots & P^{B_1=e_8, B_2=e_8} \end{pmatrix}
 \end{matrix}$$

235 Adding entries of the matrix for which branch B_1 is earlier in the tree than branch B_2 thus gives the
 236 probability that mutation 1 occurs before mutation 2. To measure the uncertainty of the ordering of the
 237 mutations, we rank all possible mutation orders by their posterior probabilities, and construct a $(1-\theta) \times 100\%$
 238 credible set by adding orders with decreasing probability until the sum exceeds $1 - \theta$. The MAP estimator
 239 for the order of I mutations is thus given by

$$\hat{\mathcal{B}}_{MAP} = \underset{\mathcal{B} \in \{e_1, \dots, e_{2J-2}\}^I}{\operatorname{argmax}} P(\mathcal{B} | \mathbf{S}, \mathcal{T}, \mathbf{N}, \mathcal{Q}_\lambda). \tag{2.20}$$

240

3. SIMULATION STUDY

241 To evaluate the ability of our method, which we call MO (Mutation Order), to correctly identify the locations
 242 and the order of a set of mutations under different conditions, we conduct a series of simulation studies with
 243 data simulated under different assumptions. The goal is to assess the effect of data quality (complete or
 244 incomplete, high or low error probabilities), number of cells, branch lengths, number of mutations and type
 245 of genotype data on the performance of our method. We consider a total of 12 scenarios, with 100 replicates
 246 for each setting within each scenario. Scenarios 1 - 4 involve data generated under our model for either 10
 247 cells (scenarios 1 and 2) or 50 cells (scenarios 3 and 4) for either long branch lengths (scenarios 1 and 3)
 248 or short branch lengths (scenarios 2 and 4). Scenarios 5 - 8 consider data simulated under various models
 249 implemented in the CellCoal software (Posada, 2020). Scenarios 9 and 10 involve data generated under
 250 our model, but with mutations placed on branches with varying (rather than equal) probabilities. Finally,
 251 scenarios 11 and 12 consider data simulated under the finite sites assumption (all other simulation settings

252 use the infinite sites assumption). The methods used to simulate data under these different scenarios are
253 described in detail in Section A of the Supplementary Material, and Section D of the Supplementary Material
254 provides information about computational requirements.

255 3.1 *Accuracy of MAP estimates*

256 We assess the accuracy of the MAP estimates in MO across the 100 trees within each simulation setting in
257 several ways, including whether the mutation is inferred to occur on the correct branch (“location accuracy”),
258 whether any pair of mutations are inferred to occur in the correct order (“order accuracy”), and whether a
259 pair of mutations that occur on adjacent branches are inferred to occur in the correct order (“adjacent order
260 accuracy”). In evaluating both the order accuracy and adjacent order accuracy, if two sequential mutations
261 are inferred to occur on the same branch, then it is counted as ordering the mutations incorrectly. In addition,
262 pairs of mutations that occur on the same branch are also included in the computation of order accuracy
263 and adjacent order accuracy. The details of how the MAP estimates are assessed are given in Section B of
264 the Supplementary Material. Tables 1 to 4 in the Supplementary Material show the location accuracy for
265 scenarios 1 to 4 with each cell entry corresponding to a unique setting of α , β , type of genotype and missing
266 data percentage. In most cases, the location accuracy of MO is high except when the error probabilities are
267 high. The accuracy rates of settings with 50 cells in Tables 3 and 4 are slightly higher than those with 10
268 cells in Tables 1 and 2. With the same type of genotype and same error probability setting, the accuracy
269 decreases as the percentage of missing values increases. When α (or β) is fixed, accuracy decreases as β (or
270 α) increases.

271 The results for order accuracy (Tables 5 to 8 in the Supplementary Material) and adjacent order accuracy
272 (Tables 9 to 12 in the Supplementary Material) for scenarios 1 to 4 are similar. In addition to the same overall
273 trend due to number of cells, data type, percentage of missing data and error probabilities, the order accuracy
274 rates are higher than the corresponding adjacent order accuracy rates.

275 The results for location accuracy, order accuracy and adjacent order accuracy of MO in scenarios 5 to
276 10 have similar patterns to those observed for scenarios 1 to 4. The accuracy in scenarios 5 to 10 is not
277 affected by the number of mutations. In addition to the same overall trend due to the number of cells, type
278 of genotype, missing data percentage and error probabilities, the accuracy rates in scenarios 5 to 10 are

279 higher than the corresponding accuracy rates in scenarios 1 to 4. Especially when error probabilities are low,
280 the accuracy can be as high as 99%.

281

3.2 *Credible set accuracy*

282 The credible set accuracy of the inferred mutation branch is assessed as well. If the true mutation branch
283 is within the credible set, we count this as correct; otherwise, it is incorrect. We use 95% credible set
284 for computation (Tables 13 to 16 for scenarios 1 to 4 in the Supplementary Material). The credible set
285 accuracy has the same overall trend as the accuracy of MAP estimates due to the number of cells, type of
286 genotype, missing data percentage and error probabilities, though the accuracy is much higher than that
287 of the corresponding MAP estimates, especially for settings with large error probabilities and high missing
288 data percentages. The overall trend for scenarios 5 to 10 is similar to scenarios 1 to 4, but the corresponding
289 accuracy rates in scenarios 5 to 10 are higher than those in scenarios 1 to 4.

290

3.3 *Comparison with competing approaches*

291 To further assess the performance of MO, we compare its performance with the methods SCITE (Jahn *and*
292 *others*, 2016) and SiFit (Zafar *and others*, 2017) for the simulation data in scenarios 1 to 12. SCITE can
293 estimate the order of mutations for either binary or ternary genotype data. We use the maximum likelihood
294 mutation order inferred by SCITE with 1,000,000 iterations given the true error probabilities. SiFit can
295 use either binary or ternary genotype data when inferring the phylogenetic tree, but it can only use binary
296 genotype data when inferring mutation order. We estimate the most likely mutational profiles for the tips
297 and the internal nodes by SiFit given the true phylogenetic tree, error probabilities and mutation rates. We
298 then extract the mutation order information from the output. The three methods are compared with respect
299 to the order accuracy and adjacent order accuracy for the above simulation settings.

300 3.3.1 *Scenarios 1 to 4* Fig. 3 and Fig. 4 plot the order accuracy and the adjacent order accuracy for the
301 three methods in scenarios 1 to 2, respectively. Fig. S2 and Fig. S3 in the Supplementary Material plot the
302 order accuracy and the adjacent order accuracy for the three methods in scenarios 3 to 4, respectively. In
303 each figure, the top row shows the results for binary data and the bottom row shows the results for ternary
304 data. In each panel, different methods are highlighted in different colors.

305 In scenarios 1 to 4, order accuracy and adjacent order accuracy show decreasing trend as data quality
306 becomes worse for all three methods. For results estimated from the trees with 10 cells (scenarios 1 and

307 2), MO has slightly higher adjacent order accuracy estimated from binary and ternary data. Only when
308 both α and β are large does SCITE have higher adjacent order accuracy rates than MO. Comparing order
309 accuracy when there are 10 cells in each tree, MO has comparable order accuracy when error probabilities
310 are small. MO has lower order accuracy than SCITE when error probabilities are large but the discrepancies
311 of order accuracy rates between MO and SCITE are only 5% on average. When there are 50 cells in each tree
312 (scenarios 3 and 4), MO is superior to SCITE in all settings in terms of order accuracy and adjacent order
313 accuracy estimated from both binary and ternary genotype data. Specifically, the order accuracy for MO is
314 25% higher than SCITE on average, and the adjacent order accuracy for MO is 20% higher than SCITE
315 on average. In all settings, SiFit has the worst performance since only a subset of the input mutations are
316 inferred to occur on the tree. Although the output partial mutation order from SiFit are mostly correct,
317 the accuracy is low due to the small number of inferred mutation orders. MO thus dominates SiFit when
318 assessing the performance using order accuracy and adjacent order accuracy. Comparing between settings
319 with 10 cells and those with 50 cells, the performance of MO is consistently good, and the accuracy increases
320 as the number of cells increases. SiFit performs better as the number of cells increases as well. However, the
321 performance of SCITE becomes worse when the number of cells increases. Although the number of correct
322 pairs inferred by SCITE increases, the accuracy decreases because the total number of true pairs increases.

323 3.3.2 *Scenarios 5 to 8* Fig. S4 and Fig. S5 in the Supplementary Material plot the order accuracy and
324 adjacent order accuracy for scenarios 5 and 6, respectively. In scenarios 5 and 6 where mutations evolve by
325 the infinite sites diploid model, order accuracy and adjacent order accuracy show decreasing trend as data
326 quality becomes worse for all three methods, as is observed for scenarios 1 to 4. MO is superior to SCITE
327 in all settings in terms of adjacent order accuracy and order accuracy. In all the settings, SiFit has the
328 worst performance with respect to order accuracy. However, SiFit has comparable adjacent order accuracy
329 to SCITE when error probabilities are small. Similar to scenarios 1 to 4, only a proportion of mutations
330 are inferred to occur on the tree by SiFit. MO thus dominates SiFit in scenarios 5 and 6. In all settings for
331 scenarios 5 and 6, the number of mutations and number of tips in the tree do not affect the order accuracy
332 or adjacent order accuracy of MO and SiFit very much. However, the performance of SCITE is affected by
333 the number of mutations. As the number of mutations increases, the accuracy of SCITE becomes lower. In
334 addition, the adjacent order accuracy of SCITE increases as the number of cells increases.

335 Fig. S6 and Fig. S7 in the Supplementary Material plot the order accuracy and the adjacent order accuracy
336 for scenarios 7 and 8, respectively. In scenarios 7 and 8, mutations arise by the infinite sites diploid model,
337 as was the case for scenarios 5 and 6, but now a small proportion of the mutations are lost. Compared to the
338 complete settings in scenarios 5 and 6, the performance of all the three methods becomes worse. However,
339 the performance of the three methods is comparable to settings with missing values in scenarios 5 and 6.

340 In addition to the above comparisons, we also apply MO to data from scenarios 5 and 6 when transition
341 rates are misspecified. Fig. S11 and Fig. S12 show the order accuracy and adjacent order accuracy when
342 MO is applied with misspecified transition rates. In each panel, MO, SCITE, and SiFit are highlighted in
343 red, blue, and green, respectively, when the transition rates $\lambda_1 = 1$ and $\lambda_2 = 0$ are used, as in the initial
344 analysis in scenarios 5 and 6. Purple color corresponds to MO when the misspecified transition rates are
345 used. The performance of SCITE is not affected by misspecified transition rates. Comparing the plots, we
346 see that when binary data are used, the effect of misspecified transition rates are ignorable. However, when
347 using ternary data, the differences are noticeable. In scenario 5, the order accuracy for MO with misspecified
348 transition rates is comparable to SCITE when error probabilities are small and higher than SCITE when
349 error probabilities are large. In scenario 6, the order accuracy inferred from ternary genotype data for MO
350 with misspecified transition rates is lower than SCITE. Comparing the adjacent order accuracy with ternary
351 data, the performance of MO with the misspecified transition rates is worse than when the transition rates
352 are correctly specified in MO, but MO still performs better than SCITE.

353 3.3.3 *Scenarios 9 to 10* In scenarios 9 and 10, mutations are simulated under the mutation process
354 defined in Section 2.2. Although the transition rates are the same as in scenarios 1 to 4, each mutation is
355 not equally likely to occur on all of the branches. In Fig. S8 and Fig. S9, we observe that MO has higher
356 accuracy than SCITE and SiFit in all settings in terms of both order accuracy and adjacent order accuracy.

357 3.3.4 *Scenarios 11 to 12* In scenarios 11 and 12, mutations are simulated under the finite sites assump-
358 tion. Because it is unclear how mutation order should be defined when mutations can arise multiple times
359 along a phylogeny, we instead plot the location accuracy of MO and SiFit in Fig. S10. When there are only 10
360 tips in the tree, most simulated mutations occur only once along the tree and MO has higher accuracy than
361 SiFit. However, when there are 50 tips, most are back mutations and/or parallel mutations. SiFit performs
362 better than MO when the rate of mutating from 1 to 0 is low. When the rate of mutating from 1 to 0 is

363 high, neither MO nor SiFit identify the correct mutation location. MO is limited by its assumption that all
364 mutations occur only once on the tree. Although SiFit can infer parallel/back mutations, it is not able to
365 identify all the locations on which the mutations occur for the simulated data.

366 4. EMPIRICAL EXAMPLES

367 We apply MO to two experimental single-cell DNA sequencing datasets, one for prostate cancer (Su *and*
368 *others*, 2018) and one for metastatic colorectal cancer patients (Leung *and others*, 2017). For the prostate
369 cancer dataset, we retrieve publicly available data from the single-cell study of Su *and others* (2018), which
370 includes 10 single-cell genomes for each patient. For the colorectal cancer dataset, we use the somatic single
371 nucleotide variants (SNVs) after variant calling provided in the original study (16 SNVs for patient CRC1
372 and 36 SNVs for patient CRC2) of Leung *and others* (2017).

373 4.1 Prostate cancer data

374 4.1.1 *Data analysis* To infer tumor evolutionary trees for patients 1 and 2 (labeled P1 and P2), we
375 use the SVDQuartets method of Chifman and Kubatko (2014) as implemented in PAUP* (Swofford, 1999)
376 using the aligned DNA sequences for all somatic mutations as input with the expected rank of the flattening
377 matrix set to 4. We specify the normal cell sample as the outgroup. We use the maximum likelihood method
378 to estimate the branch lengths.

379 We select common tumor suppressor genes and oncogenes for both P1 and P2 identified by Su *and others*
380 (2018). In addition to these common cancer-associated genes across different cancers, we map mutations in
381 prostate cancer-specific genes (genes that are more commonly mutated in prostate cancer patients) suggested
382 by Barbieri *and others* (2013) and Tate *and others* (2018). For both binary and ternary genotype data for
383 these genes, we use MO to compute the posterior probability of mutation on each branch of the tumor
384 phylogeny for each of the two patients. Su *and others* (2018) estimated the error probabilities to be $(\alpha, \beta) =$
385 $(0.29, 0.02)$ for P1, and $(\alpha, \beta) = (0.31, 0.02)$ for P2. Although our method in Section 2 allows the assignment
386 of varying error probabilities across genomic sites and cells, here we use same probabilities for all sites.

387 To examine the effect of informativeness of the prior distribution on the resulting inference, we consider
388 two prior distributions for each parameter with mean equal to the estimated error probability from the
389 empirical data and with either a large or a small variance as described in Section C in the Supplementary
390 Material. For P1, we consider $\alpha|\mathbf{S}_i \sim \text{Beta}(0.29, 0.71)$ (larger variance) and $\alpha|\mathbf{S}_i \sim \text{Beta}(2.9, 7.1)$ (smaller

391 variance). For P2, we consider $\alpha|\mathbf{S}_i \sim \text{Beta}(0.31, 0.69)$ (larger variance) and $\alpha|\mathbf{S}_i \sim \text{Beta}(3.1, 6.9)$ (smaller
392 variance). For β for both P1 and P2, we consider $\beta|\mathbf{S}_i \sim \text{Beta}(0.02, 0.98)$ (larger variance) and $\beta|\mathbf{S}_i \sim$
393 $\text{Beta}(0.2, 9.8)$ (smaller variance).

394 According to Iwasa *and others* (2004), the mutation rates for the first and second mutation are estimated
395 to be $\lambda_1 = 10^{-7}$ and $\lambda_2 = 10^{-2}$, respectively. We use these values to specify the prior distributions for
396 the transition rates. Similar to the sequencing error probabilities, we set two prior distributions for each
397 transition rate with equal means but different variances. The distribution of the transition rate λ_1 ($0 \rightarrow 1$
398 for ternary genotype) is set as $\lambda_1|\mathbf{S}_i \sim \text{Gamma}(2, 5.0 \times 10^{-8})$ (larger variance) and $\lambda_1|\mathbf{S}_i \sim \text{Gamma}(5, 2.0 \times$
399 $10^{-8})$ (smaller variance). The distribution of the transition rate λ_2 ($1 \rightarrow 2$ for ternary genotype) is set as
400 $\lambda_2|\mathbf{S}_i \sim \text{Gamma}(2, 5.0 \times 10^{-3})$ (larger variance) and $\lambda_2|\mathbf{S}_i \sim \text{Gamma}(5, 2.0 \times 10^{-3})$ (smaller variance). The
401 estimated probabilities of mutation do not vary substantially when the prior distributions with larger or
402 smaller variance are used for any of these parameters. The heatmaps of estimated probabilities with different
403 prior distributions (larger or smaller variance) are in the Supplementary Material.

404 4.1.2 **Results** Fig. 5 and Fig. S13 show the tumor evolutionary tree estimated for P1 and P2, respectively.
405 In both tumor trees, the trunk connects the tumor clone to the normal clone. We annotate the genes on
406 their inferred mutation branches. The uncertainty in the inferred mutation locations is highlighted in colors.
407 Mutations with strong signal (defined to be a posterior probability larger than 0.7 that the mutation occurred
408 on a single branch) are colored red, while mutations with moderate signal (defined to be a total posterior
409 probability larger than 0.7 on two or three branches) are colored blue. Note that the posterior probability
410 on a branch measures the support in the data under the model and prior distribution for the placement of
411 the mutation on that branch. Mutations colored red are those for which the placement on a single branch
412 is strongly supported. Mutations colored blue are those for which there is strong support for the mutation
413 having occurred on one of the indicated branches. This should not be interpreted as evidence that the
414 mutation occurred more than once; rather, it means that the precise placement of the mutation is ambiguous
415 but can be confidently limited to the branches indicated.

416 We also compare the estimated posterior probability distributions for mutations of common cancer-
417 associated genes for patients P1 and P2, which are used to construct credible sets and to measure the
418 uncertainty of the inferred mutation order. Fig. S16 to Fig. S19 are the posterior probability distribution

419 heatmaps for patients P1 and P2 with different prior distributions (larger or smaller variance).

420 Fig. S20 to Fig. S23 show heatmaps of the estimated posterior probabilities for prostate cancer-specific
421 genes for patients P1 and P2 with different prior distributions (larger or smaller variance). In agreement with
422 the results of Su et al. (2018), we find that mutation of *TP53*, which is commonly associated with tumor
423 initiation in many cancers (see, e.g., Yu and others (2014)), is inferred to occur on the trunk of the tree with
424 high probability in patient P1, but not on the trunk of the tumor tree of patient P2. Gene *ZFH3* has a
425 high probability of having mutated on the trunk of the tree in both patients. In addition, the heatmap for
426 patient P1 shows strong signal that *FOXP1* mutates on the trunk of the tumor tree, while *BRCA2* has a high
427 probability of having mutated on the trunk of the tree for patient P2. Comparing the heatmaps of common
428 cancer-associated genes with the prostate cancer-specific genes, mutations inferred to have occurred on the
429 trunk of the tree tend to be those that are common across cancer types, while mutations known to have high
430 frequency within prostate cancer are generally found closer to the tips of the tree in both patients.

431 4.2 Metastatic colorectal cancer data

432 4.2.1 *Data analysis* The original study of Leung and others (2017) reported 16 and 36 SNVs for patients
433 CRC1 and CRC2 after variant calling. We use SiFit (Zafar and others, 2017) to estimate each colorectal
434 patient's tumor phylogeny, including branch lengths, since there are fewer data available to estimate the
435 phylogenies in this case and this method is specifically designed to estimate tumor phylogenies from single-
436 cell data. The normal cells in each patient are merged into one normal sample and used as the outgroup.

437 Leung and others (2017) reported error probabilities of $(\alpha, \beta) = (0.0152, 0.0789)$ and $(\alpha, \beta) = (0.0174, 0.1256)$
438 for CRC1 and CRC2, respectively. For each patient, we use these values to specify the same prior distri-
439 butions across all sites. For CRC1, we consider $\alpha|\mathbf{S}_i \sim \text{Beta}(0.0152, 0.9848)$ (larger variance) and $\alpha|\mathbf{S}_i \sim$
440 $\text{Beta}(0.15, 9.85)$ (smaller variance); and $\beta|\mathbf{s}_i \sim \text{Beta}(0.078, 0.922)$ (larger variance) and $\beta|\mathbf{S}_i \sim \text{Beta}(0.78, 9.22)$
441 (smaller variance). For CRC2, we consider $\alpha|\mathbf{S}_i \sim \text{Beta}(0.0174, 0.9826)$ (larger variance) and $\alpha|\mathbf{S}_i \sim \text{Beta}(0.174, 9.826)$
442 (smaller variance); and $\beta|\mathbf{S}_i \sim \text{Beta}(0.1256, 0.8744)$ (larger variance) and $\beta|\mathbf{S}_i \sim \text{Beta}(1.256, 8.744)$ (smaller
443 variance). The prior distributions for the transition rates for CRC1 and CRC2 are estimated by SiFit. As
444 was found for the prostate cancer patients, the estimated probabilities do not vary substantially when we
445 use prior distributions with small or large variance.

446 4.2.2 **Results** The inferred tumor trees and mutation order are depicted in Fig. S14 and Fig. S15 in the
447 Supplementary Material. The posterior probabilities of the inferred mutation locations are indicated with
448 colors as for the prostate cancer data, and agree overall with the findings of Leung *and others* (2017). Fig. S24
449 and Fig. S25 are heatmaps for the posterior probability distribution of each mutation for patients CRC1 and
450 CRC2 with different priors. For patient CRC1, mutations in *APC*, *KRAS* and *TP53* are inferred to have been
451 acquired on the trunk of the tumor phylogeny with high posterior probability, in agreement with Leung *and*
452 *others* (2017) and in agreement with past studies. The studies of Fearon and Vogelstein (1990) and Powell
453 *and others* (1992) have shown that the mutation order of these genes appears to be fixed in initializing
454 colorectal cancer, providing further support for our findings. In addition, we identify the five mutations
455 specific to metastatic cells that are found by Leung *and others* (2017), with three (*ZNF521*, *TRRAP*, *EYS*)
456 inferred to occur on branch 97 in Fig. S14. Support is found for placement of *RBFOX1* and *GATA1* in two
457 distinct regions of the tree. Each supported placement is on a branch that leads to a clade of metastatic
458 aneuploid cells, indicating the association of such cells with these mutations. If the tree is correct, then this
459 might indicate that these mutations arose more than once (though our model assumes that each mutation
460 only arose once, if the “truth” is that the mutation arose more than once, a reasonable behavior of our model
461 would be to partition the posterior probability between the two origins). Another possibility is that the tree
462 is incorrect, and the two clades of metastatic aneuploid cells should actually be clustered together, which
463 would then presumably result in strong support for the placement of these mutations on the branch leading
464 to the combined clade.

465 For CRC2, we identify strong signals on branch 36 in Fig. S15 for several genes reported by Leung
466 *and others* (2017) that are shared by primary and metastatic cells, including driver mutations in *APC*,
467 *NRAS*, *CDK4* and *TP53*. We also identify an independent lineage of primary diploid cells (colored in pink in
468 Fig. S15) that evolved in parallel with the rest of the tumor with moderate to strong signals for mutations in
469 *ALK*, *ATR*, *EPHB6*, *NR3C2* and *SPEN* and that do not share the mutations listed in the previous sentence.
470 Our analysis further agrees with that of Leung *and others* (2017) in that we also identify the subsequent
471 formation of independent metastatic lineages. For example, on branches 56 and 58 we find moderate support
472 for mutations in *FUS*; and strong support for mutation on branch 136 in *HELZ* and branch 78 in *PRKCB*.
473 Many of the genes showing weaker or moderate support for mutation in these metastatic lineages agree

474 with those identified by Leung *and others* (2017). The primary difference between our result and that of
475 Leung *and others* (2017) is that we identify mutation in *NR4A3* and *FUS* to have occurred along a different
476 metastatic lineage than the mutations in *TSHZ3* and *PRKCB*.

477

5. DISCUSSION

478 Development of computational tools based on a phylogenetic framework for use in studying cancer evolution
479 has the potential to provide tremendous insight into the mechanisms that lead to ITH, especially the role
480 of the temporal order of mutations in cancer progression. For example, Ortmann et al. (2015) have shown
481 differences in clinical features and the response to treatment for patients with different mutation orders,
482 indicating that inference of the order in which mutations arise within an individual's tumor may have
483 direct implications in clinical oncology, for both diagnostic applications in measuring the extent of ITH and
484 targeted therapy. SCS data provide an unprecedented opportunity to estimate mutation order at the highest
485 resolution. However, such data are subject to extensive technical errors that arise during the process of
486 whole-genome amplification.

487 To analyze such data, we introduce MO, a new Bayesian approach for reconstructing the ordering of
488 mutational events from the imperfect mutation profiles of single cells. MO is designed to infer the temporal
489 order of a collection of mutations of interest based on a phylogeny of cell lineages that allows modeling of the
490 errors at each tip. MO can infer the mutation order that best fits single-cell data sets that are subject to the
491 technical noise, including ADO, false positive errors, low-quality data, and missing data. The assumption of
492 independence of mutations made by MO is the same as that made in other methods developed for inferring
493 mutation order (e.g., Zafar *and others* (2017), Zafar *and others* (2019), and Jahn *and others* (2016)). Thus,
494 MO does not presently account for possible interactions between the occurrences of mutations, though
495 it could be extended to accommodate this if biological information about these interactions is available.
496 However, recent work (Canisius *and others*, 2016) indicates that observed dependence typically takes the
497 form of mutual exclusivity (i.e., only one gene in the group will be mutated in any given patient) rather than
498 positive association, making the independence assumption of less concern here, as the set of mutations we
499 study are assumed to be present within an individual patient. MO could also be extended to work on clonal
500 trees and models that include errors in observed data for multiple cells in a tip instead of a single cell. In
501 addition, MO could be modified to account for the accelerated mutation rates common in late-stage cancers,

502 or to allow for back or parallel mutation.

503 An important difference between MO and existing methods, such as SCITE (Jahn *and others*, 2016) and
504 SiFit (Zafar *and others*, 2017), is the mechanism for quantifying uncertainty in the inferred order. Options
505 available within SCITE (Jahn *and others*, 2016) allow for estimation of the posterior probability distribution
506 across orders. SiFit (Zafar *and others*, 2017), on the other hand, could be modified to account for uncertainty
507 in the orders because the true tumor phylogeny is unknown and must first be estimated. In contrast, because
508 MO uses a probabilistic model for inferring mutation locations along a fixed tree, it is able to provide an
509 estimate of uncertainty in the inferred locations conditioning on the correct tumor phylogeny, thus capturing
510 a source of uncertainty that differs from what SCITE and SiFit provide. MO performs accurately, as is
511 evident from a comprehensive set of simulation studies that take into account different aspects of modern
512 SCS data sets by examining a wide range of error probabilities, fractions of missing data, branch lengths, and
513 numbers of cells in each tree. The simulation studies also demonstrate that MO outperforms the state-of-the-
514 art methods when the number of cells is large and performs comparably to other methods when the number
515 of cells is small. MO is robust to the technical errors that arise during whole-genome amplification. When
516 applied to data from prostate cancer patients and colorectal cancer patients, MO is able to not only provide
517 insight into the locations of cancer-associated mutations, but also the level of certainty in the locations.
518 However, MO does not provide estimates of transition rates and error probabilities as SiFit and SCITE do,
519 but rather integrates over uncertainty in these parameters.

520 The methodology underlying MO could be enhanced by incorporating models for copy number alterations,
521 as well as by considering mutations that affect the same allele more than once. As SCS data collection becomes
522 more advanced, enabling hundreds of cells to be analyzed in parallel at reduced cost and increased throughput,
523 MO is poised to analyze the resulting large-scale data sets to make meaningful inference of the mutation
524 order during tumor progression for individual patients. MO thus represents an important step forward in
525 understanding the role of mutation order in cancer evolution and as such may have important translational
526 applications for improving cancer diagnosis, treatment, and personalized therapy. If inferred mutation order
527 can be associated with clinical outcomes, future research can explore the cause of clinical outcomes given
528 specific mutation order with the goal of developing novel targeted treatments. This will allow clinical providers
529 to make decisions concerning treatment based on the mutation landscapes of patients. Although the current

REFERENCES

23

530 study focuses on cancer, MO can potentially also be applied to single-cell mutation profiles from a wide
531 variety of fields. These applications are expected to provide new insights into our understanding of cancer
532 and other human diseases.

533

6. SOFTWARE

534 MO has been implemented in R and is available at <https://github.com/lkubatko/MO>.

535

7. SUPPLEMENTARY MATERIAL

536 Supplementary material is available.

537

8. ACKNOWLEDGMENTS

538 The simulation experiments and data analyses were carried out using the ASC Unity Cluster at The Ohio
539 State University, USA. The authors thank two anonymous reviewers for helpful comments on an earlier draft
540 of this manuscript.

541 *Conflict of Interest:* None

542

REFERENCES

543 ASCOLANI, GIANLUCA AND LIÒ, PIETRO. (2019). Modeling breast cancer progression to bone: how driver
544 mutation order and metabolism matter. *BMC Medical Genomics* **12**(6), 106.

545 BARBIERI, CHRISTOPHER E, BANGMA, CHRIS H, BJARTELL, ANDERS, CATTO, JAMES WF, CULIG, ZO-
546 RAN, GRÖNBERG, HENRIK, LUO, JUN, VISAKORPI, TAPIO AND RUBIN, MARK A. (2013). The mutational
547 landscape of prostate cancer. *European Urology* **64**(4), 567–576.

548 CANISIUS, SANDER, MARTENS, JOHN W. M. AND WESSELS, LODEWYK F. A. (2016). A novel independence
549 test for somatic alterations in cancer shows that biology drives mutual exclusivity but chance explains most
550 co-occurrence. *Genome Biology* **17**, 261.

551 CHIFMAN, JULIA AND KUBATKO, LAURA. (2014). Quartet inference from SNP data under the coalescent
552 model. *Bioinformatics* **30**(23), 3317–3324.

553 FEARON, ERIC R AND VOGELSTEIN, BERT. (1990). A genetic model for colorectal tumorigenesis. *cell* **61**(5),
554 759–767.

- 555 ISHWARAN, HEMANT, BLACKSTONE, EUGENE H, APPERSON-HANSEN, CAROLYN AND RICE, THOMAS W.
556 (2009). A novel approach to cancer staging: application to esophageal cancer. *Biostatistics* **10**(4), 603–620.
- 557 IWASA, YOH, MICHOR, FRANZISKA AND NOWAK, MARTIN A. (2004). Stochastic tunnels in evolutionary
558 dynamics. *Genetics* **166**(3), 1571–1579.
- 559 JAHN, KATHARINA, KUIPERS, JACK AND BEERENWINKEL, NIKO. (2016). Tree inference for single-cell data.
560 *Genome Biology* **17**(1), 86.
- 561 JAMAL-HANJANI, MARIAM, WILSON, GARETH A, MCGRANAHAN, NICHOLAS, BIRKBAK, NICOLAI J,
562 WATKINS, THOMAS BK, VEERIAH, SELVARAJU, SHAFI, SEEMA, JOHNSON, DIANA H, MITTER,
563 RICHARD, ROSENTHAL, RACHEL *and others*. (2017). Tracking the evolution of non-small-cell lung cancer.
564 *New England Journal of Medicine* **376**(22), 2109–2121.
- 565 KIM, KYUNG IN AND SIMON, RICHARD. (2014). Using single cell sequencing data to model the evolutionary
566 history of a tumor. *BMC Bioinformatics* **15**(1), 27.
- 567 LEUNG, MARCO L., DAVIS, ALEXANDER, GAO, RULI, CASASENT, ANNA, WANG, YONG, SEI, EMI, VILAR,
568 EDUARDO, MARU, DIPEN, KOPETZ, SCOTT AND NAVIN, NICHOLAS E. (2017). Single-cell DNA sequenc-
569 ing reveals a late-dissemination model in metastatic colorectal cancer. *Genome Research* **27**, 1287–1299.
- 570 NAVIN, NICHOLAS E. (2014). Cancer genomics: one cell at a time. *Genome Biology* **15**(8), 452.
- 571 ORTMANN, CHRISTINA A, KENT, DAVID G, NANGALIA, JYOTI, SILBER, YVONNE, WEDGE, DAVID C,
572 GRINFELD, JACOB, BAXTER, E JOANNA, MASSIE, CHARLES E, PAPAEMMANUIL, ELLI, MENON, SURAJ
573 *and others*. (2015). Effect of mutation order on myeloproliferative neoplasms. *New England Journal of*
574 *Medicine* **372**(7), 601–612.
- 575 O’SULLIVAN, FINBARR, ROY, SUPRATIK AND EARY, JANET. (2003). A statistical measure of tissue hetero-
576 geneity with application to 3D PET sarcoma data. *Biostatistics* **4**(3), 433–448.
- 577 POSADA, DAVID. (2020). CellCoal: coalescent simulation of single-cell sequencing samples. *Molecular Biology*
578 *and Evolution* **37**(5), 1535–1542.

REFERENCES

25

- 579 POWELL, STEVEN M, ZILZ, NATHAN, BEAZER-BARCLAY, YASMIN, BRYAN, TRACY M, HAMILTON, STAN-
580 LEY R, THIBODEAU, STEPHEN N, VOGELSTEIN, BERT AND KINZLER, KENNETH W. (1992). Apc muta-
581 tions occur early during colorectal tumorigenesis. *Nature* **359**(6392), 235–237.
- 582 SU, FEI, ZHANG, WEI, ZHANG, DALEI, ZHANG, YAQUN, PANG, CHENG, HUANG, YINGYING, WANG, MIAO,
583 CUI, LUWEI, HE, LEI, ZHANG, JINSONG *and others*. (2018). Spatial intratumor genomic heterogeneity
584 within localized prostate cancer revealed by single-nucleus sequencing. *European Urology* **74**(5), 551–559.
- 585 SWOFFORD, DL. (1999). Phylogenetic analysis using parsimony, PAUP* 4.0, beta version 4.0 b2. *Sinauer*
586 *Associates, Boston, Mass.*
- 587 TATE, JOHN G, BAMFORD, SALLY, JUBB, HARRY C, SONDKA, ZBYSLAW, BEARE, DAVID M, BINDAL,
588 NIDHI, BOUTSELAKIS, HARRY, COLE, CHARLOTTE G, CREATORE, CELESTINO, DAWSON, ELISABETH
589 *and others*. (2018). COSMIC: the catalogue of somatic mutations in cancer. *Nucleic Acids Re-*
590 *search* **47**(D1), D941–D947.
- 591 YU, CHANG, YU, JUN, YAO, XIAOTIAN, WU, WILLIAM K. K., LU, YOUYONG, TANG, SENWEI, LI,
592 XIANGCHUN, BAO, LI, LI, XIAOXING, HOU, YONG, WU, RENHUA, JIAN, MIN, CHEN, RUOYAN, ZHANG,
593 FAN, XU, LIXIA, FAN, FAN, HE, JUN, LIANG, QIAOYI, WANG, HONGYI, HU, XUEDA, HE, MINGHUI,
594 ZHANG, XIANG, ZHENG, HANCHENG, LI, QIBIN, WU, HANJIE, CHEN, YAN, YANG, XU, ZHU, SHIDA,
595 XU, XUN, YANG, HUANMING, WANG, JIAN, ZHANG, XIUQING, SUNG, JOSEPH J. Y., LI, YINGRUI *and*
596 *others*. (2014). Discovery of biclonal origin and a novel oncogene SLC12A5 in colon cancer by single-cell
597 sequencing. *Cell Research* **24**, 701–712.
- 598 ZAFAR, HAMIM, NAVIN, NICHOLAS, CHEN, KEN AND NAKHLEH, LUAY. (2019). SiCloneFit: Bayesian infer-
599 ence of population structure, genotype, and phylogeny of tumor clones from single-cell genome sequencing
600 data. *Genome Research* **29**, 1–13.
- 601 ZAFAR, HAMIM, TZEN, ANTHONY, NAVIN, NICHOLAS, CHEN, KEN AND NAKHLEH, LUAY. (2017). SiFit:
602 inferring tumor trees from single-cell sequencing data under finite-sites models. *Genome Biology* **18**(1),
603 178.

604

||

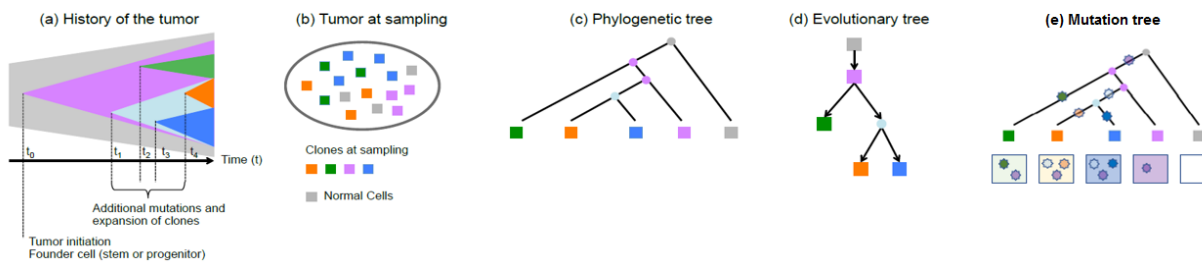


Fig. 1: Pictorial representation of tumor evolution. (a) - (b) A pictorial representation of the evolution of a tumor from the first initiating mutation to the heterogeneous tissue at the time of sampling, which consists of four different clones and normal tissue. (c) A phylogenetic tree with single cells as the tips. (d) A clonal lineage tree inferred from sampled cells where each node represents a subclone (cluster of cells). (e) A mutation tree inferred from sampled cells where each star represents the occurrence of one mutation. The box underneath each tip shows which mutations are present in the cell represented by the tip.

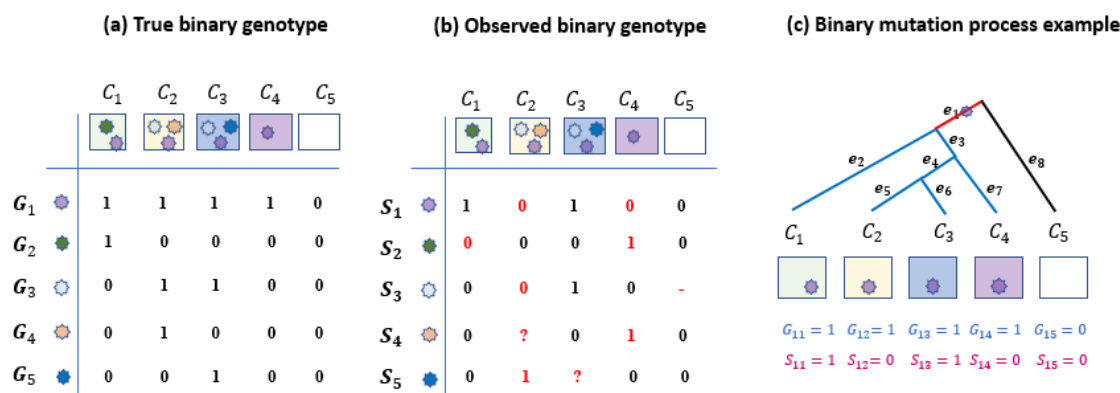
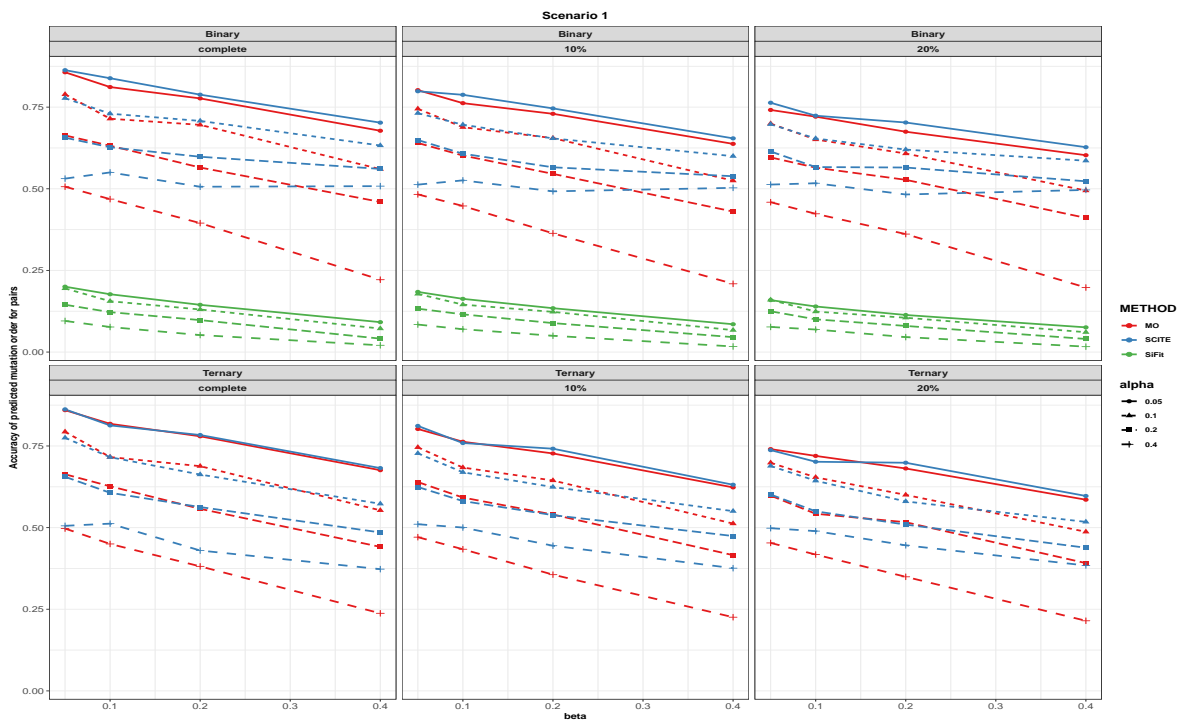
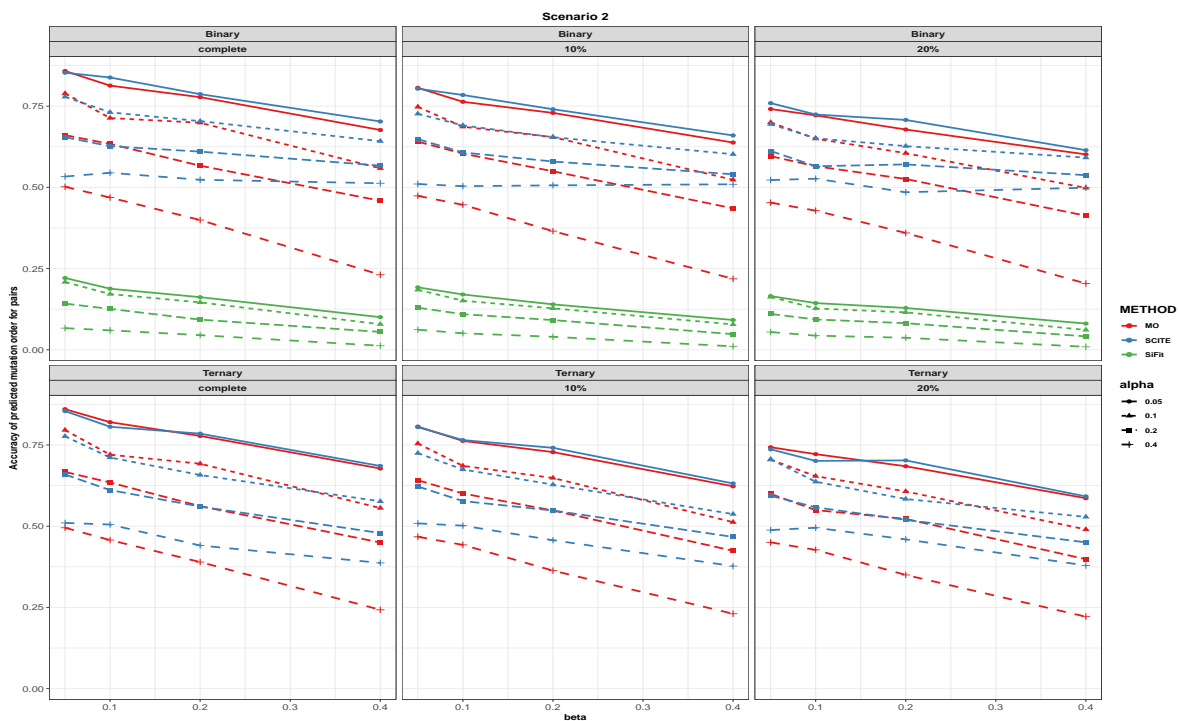


Fig. 2: True binary data, observed binary data and binary mutation process example. (a) True binary mutation matrix of the sequenced tumor cells in the mutation tree in Fig. 1(e). Each row represents true genotypes for one genomic site in all cells and each column represents the true genotypes of multiple genomic sites for one single cell. (b) Observed mutation matrix with missing and ambiguous values (red), as well as mutation states that are misrecorded with respect to the true mutation matrix (red numbers; these are either false positives or false negatives). The red dash indicates a missing value since the sequencing process does not return signal at this site of this cell, and the red question mark represents an ambiguous value. Each row represents observed states for one genomic site in all cells and each column represents the observed states of multiple genomic sites for one single cell. (c) Binary mutation process example. A mutation is acquired on branch e_1 (highlighted in red). The cell descending from branch e_8 (highlighted in black) does not carry the mutation, while the cells descending from the blue branches carry the mutation.

REFERENCES

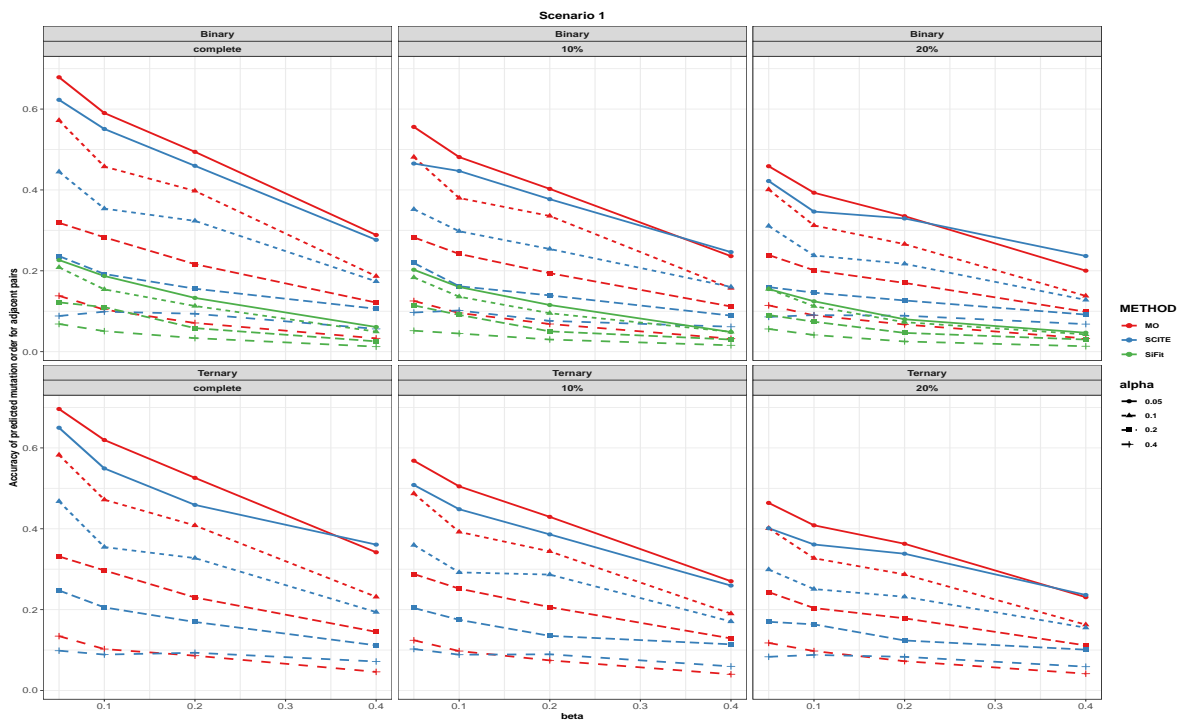


(a)

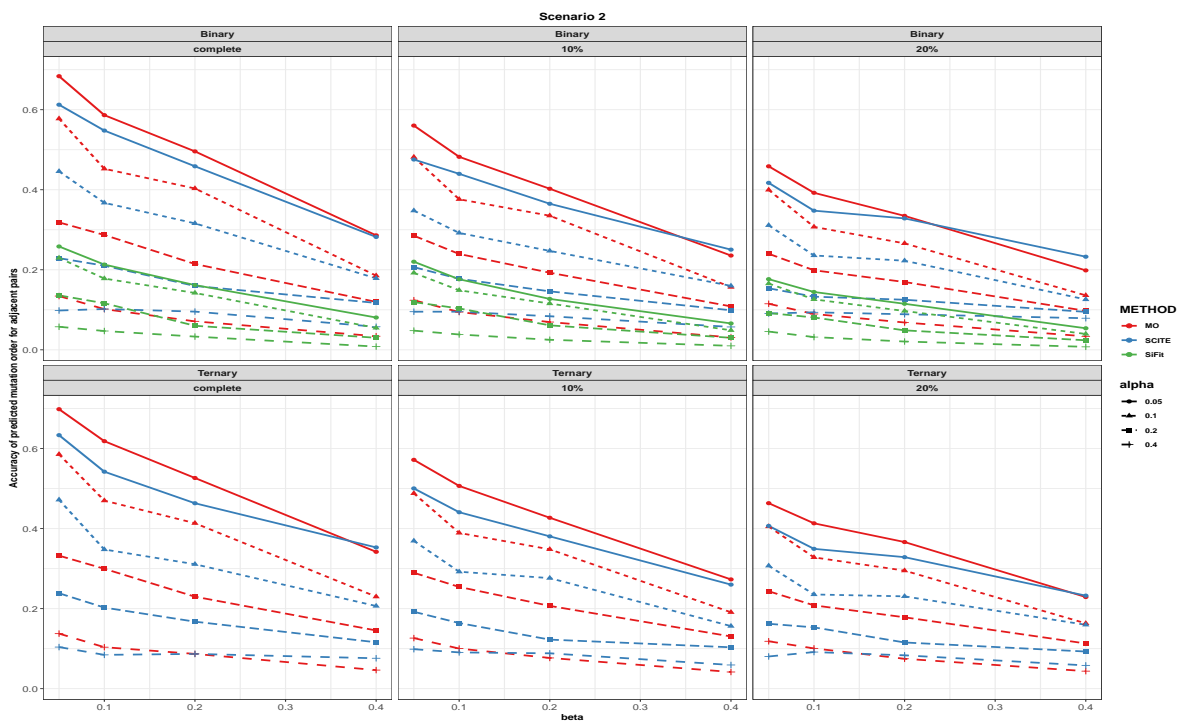


(b)

Fig. 3: Order accuracy in scenarios 1 and 2 for MO, SCITE and SiFit. Each panel includes the results from the specific type of genotype and missing data percentage. In each panel, red, blue and green colors correspond to MO, SCITE and SiFit, respectively. Each plotting symbol on the line represents a different probability of a false positive error, α . The x-axis is the probability of a false negative error, β , and the y-axis is order accuracy.



(a)



(b)

Fig. 4: Adjacent order accuracy in scenarios 1 and 2 for MO, SCITE and SiFit. Each panel includes the results from the specific type of genotype and missing data percentage. In each panel, red, blue and green colors correspond to MO, SCITE and SiFit, respectively. Each plotting symbol on the line represents a different probability of a false positive error, α . The x-axis is the probability of a false negative error, β , and the y-axis is adjacent order accuracy.

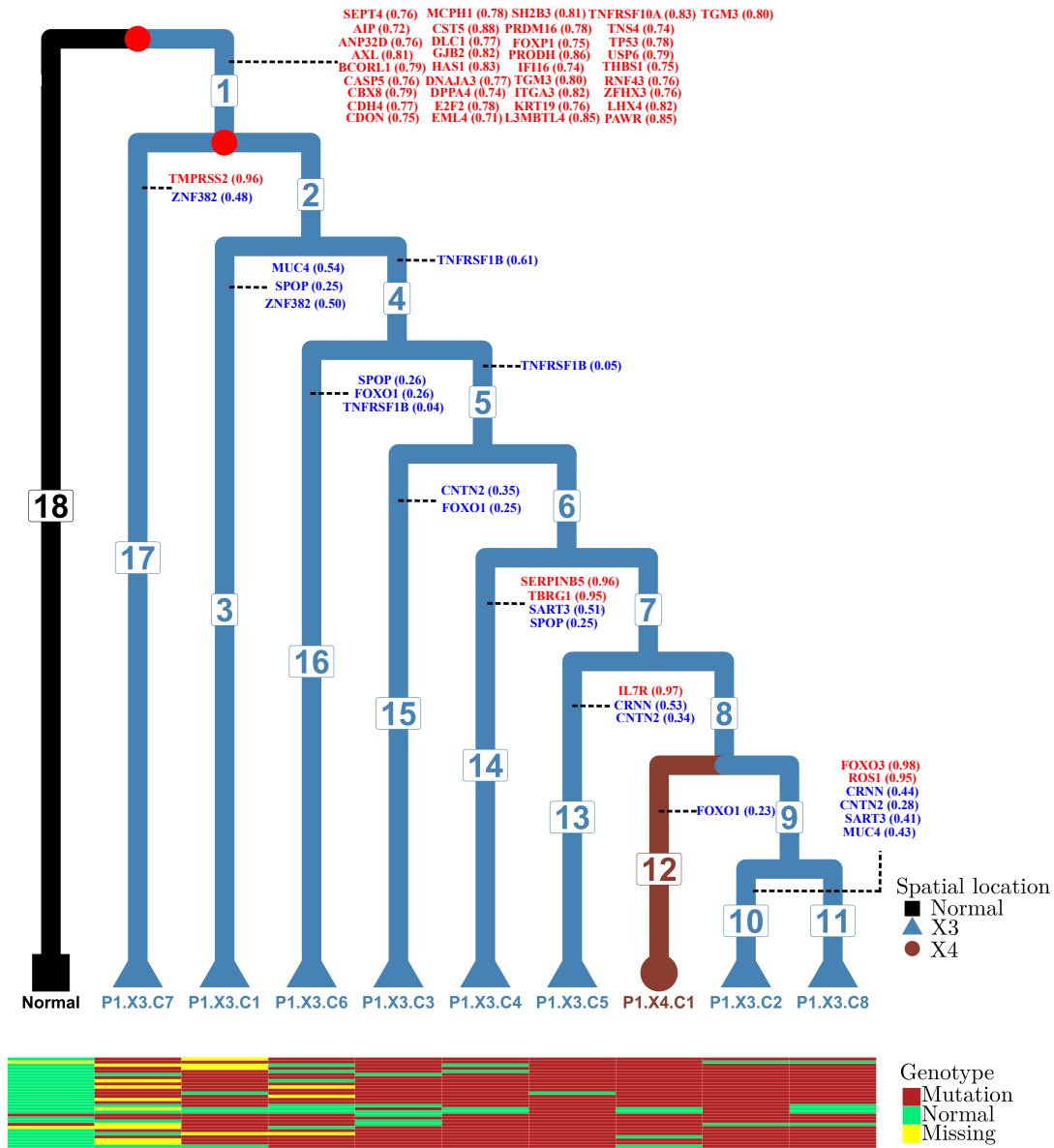


Fig. 5: P1 tumor phylogenetic tree and inferred temporal order of the mutations. The normal cell is set as the outgroup. There are 18 branches in this tree. We do not assume the molecular clock when estimating the branch lengths. Branch lengths in this figure are not drawn to scale. The color and tip shape represent the spatial locations of the samples (normal tissue, location X3 or location X4; see Su *and others* (2018)). The temporal order of the mutations is annotated on the branches of the tree. Mutations with very strong signals (probability of occurring on one branch is greater than 0.7) are highlighted in red, while mutations with moderate signals (probabilities that sum to more than 0.7 on two or three branches) are highlighted in blue. Mutation data for 30 genes corresponding to the first 30 rows in Fig. S16 and Fig. S17 for each tip are shown in the heatmap matrix at the bottom.